Article:

Circuit architecture for electrical impedance spectroscopy instrumentation to address electrode impedance mismatch in clinical devices

T Jamie Healey, *member, IEEE,* Dr Emily Rose Billinge, Dr James J.P. Alix, BSc(Hons), MBChB, MRCP and Professor Visakan Kadirkamanathan member IEEE, Charlotte. R. Kemp

Abstract— A mismatch in electrode impedance is a common and significant source of artefact in electrical impedance spectroscopy systems. We have analysed these artefacts, identifying key parameters in the optimisation of both current and voltage excited electrical impedance spectroscopy systems. We have used this information to develop a new clinical system for investigating muscle impedance anisotropy in human limbs, with the aim of developing biomarkers for various muscle pathologies. This new instrumentation integrates buffering at the front-end, which isolates the electrodes from both multiplexing and wiring parasitics. Modelling of the front-end instrumentation demonstrates an input impedance of over 1 GΩ in parallel with 0.4 pF. The clinical system currently has 16 electrodes, with the capability for more, and operates over a physiologically relevant frequency range of 76 Hz to 625 kHz. Results presented in this paper show that the new system operates with reduced levels of artefact, even in the presence of a significant mismatch in electrode impedances.

Index Terms— electrical impedance tomography, electrical impedance spectroscopy, myography, electrode impedance, instrumentation, matching, artefact reduction, tutorial
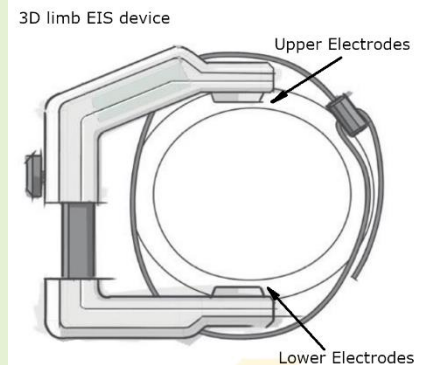
I. INTRODUCTION

Electrical impedance spectroscopy (EIS) has been successfully used for many years for the purpose of tissue characterization. Examples of clinical studies involving EIS include trials focused on developing biomarkers for disease, such as the detection of cervical intraepithelial neoplasia [1] and motor neuron disease [2]. There has also been great interest in using electrical impedance for imaging in the form of electrical impedance tomography (EIT) [3][4][5].

This paper is presented as a tutorial paper to provide the reader with a guide for the design of an EIS system and shows some aspects that require consideration for the production of such an EIS system. It would not be possible, in a single paper, to cover in detail all aspects of a full EIS system and so this paper focuses on the front-end instrumentation and its interaction with the electrode impedances. The design process for different systems may well generate radically different system architectures. Developments are made to common system models to assess interactions between the electrodes and the EIS system's front-end instrumentation. These models are then used to guide the development of an example system to take spectral measurements of the static electrical impedance of a human limb. Other EIS system design subjects, such as signal generation, demodulation, conversion and signal-to-noise ratio have been addressed by other authors (eg Wu *et al.* [28]) and will not be covered here.

In practice, electrical impedance systems must make an electrical connection to the body under test via electrodes, and electrode connections often introduce undesired impedance into the system. This impedance has contributions from the electrode system itself, body/skin surface (e.g. skin, mucous membrane) and spreading impedances, and so for simplicity, in this paper we will combine these and refer to them collectively as electrode impedance [6][7]. The electrode impedance is poorly controlled and varies between electrodes and subjects and so systems must be employed to reduce their influence on the measurements being made. One method to reduce the influence of the unknown electrode impedance is to use a four-port impedance measurement to measure the properties of the tissue of interest. Unfortunately, this technique does not fully

remove the artefact caused by the electrode impedances. Many researchers [8][9] have looked at the interaction of practical instrumentation with finite electrode impedance. In this paper, we extend this work to address mismatches between electrode impedances. Also we demonstrate that the assumption of balanced impedances is not suitable, but if a number of simplifications are made, then straightforward approaches may be used to analyze unbalanced electrode impedances effectively. By making a number of approximations, we have developed some simple equations that provide insight into the salient instrumentation features required to minimize the artefact caused by electrode impedance mismatch. The insights yielded by these equations include the requirement to maximize input impedance of the voltage measurement channel for voltage excited systems whereas for current excited systems, there is a more complex interaction of the current source Norton impedance and the voltage channel input impedance. To provide this, the authors have developed an instrumentation architecture that uses bootstrapping techniques to increase input impedance and integrates this with a cross-point switch that multiplexes the electrodes to the instrumentation.

We have developed a device incorporating this architecture, herein referred to as the 3D limb EIS device, which is currently undergoing a clinical trial. Preliminary data from both saline bath measurements and a human subject collected using the 3D limb EIS device are presented in support of our approach.

II. BACKGROUND TO EIS SYSTEMS

A. Types of excitation

This paper explores two general styles of electrical impedance spectroscopy system: those that are excited by a current source and those excited by a voltage source. Other workers have used impedance meters to achieve impedance spectroscopy of biological tissue Torrents *et al.* [10] and have proposed methods that can be used to mitigate some of the limitations of an impedance meter approach. The methods proposed in [10] do not, however, correct errors caused by electrode impedance mismatches. The authors note with concern that some researchers [11] have used laboratory instruments on volunteers with no mention of the required electrical isolation for patient safety, as required by the standard BS EN IEC 60601 [12]. Laboratory instruments with a simple fault of a poor earth connection can expose a patient to a dangerous level of leakage current and so compliance with BS EN IEC 60601 should be considered essential in ensuring adequate volunteer/patient safety in these situations.

The advantages and disadvantages of current and voltage excitation systems are explored in this paper. In both systems, the transfer impedance is determined by the ratio of the output voltage to the input current.

B. Current mode excitation systems

Current excitation is a common approach to measure impedances [13], this is logical as, if a system is driven with a current source where the measured output voltage divided by the input current gives the impedance. In the case of the tetrapolar system illustrated in Figure 1.a, the result gives the transfer impedance. This circuit is a balanced differential system, with equal current source and sinks (i_a and i_b), and the

output is the difference between V_{oa} and V_{ob}. The impedance Z_x is the impedance of interest (to be measured), Z_{eQ} to Z_{eT} represents the undesired, but unavoidable, electrode impedance. A simplified Cole-Cole circuit, as illustrated in Figure 1.b, is commonly used [14] to model the system element behaviour and we have used it for both electrodes and Z_x. Many researchers [6][10][27] analyse the effect of the electrode impedances; however, their modelling assumes that the electrode impedances are balanced, i.e. are the same for all electrodes and this paper will concentrate on the effects of mismatch in electrode impedances.

For the current driven system, illustrated in, Figure 1.a the input current to the body is given by the output current of the current source. The system is excited by two balanced current sources driving current into electrodes E_Q and E_S. Z_{na} and Z_{nb} model non-ideal finite current source Norton output impedance. Z_{eQ}, Z_{eR}, Z_{eS} and Z_{eT} represent the impedance of the electrode tissue interface; this interface includes the effects of the electrochemical interface where the conduction transforms from electronic to ionic at the electrode, in addition to the spreading impedance within the tissue. In principle, all the current from the current sources is applied to the impedance Z_x. In reality, no current source is perfect, and any practical current source will have residual Norton output impedance (Z_{na} and Z_{nb}) forming a current divider with the sum of impedances Z_{eQ}, Z_x, and Z_{eS}. Current shunted through Z_{na} and Z_{nb} will not flow through Z_x and hence will reduce the voltage across Z_x and introduce measurement errors. Similar errors are also introduced by current shunted by R_{La} and R_{Lb}. For voltage measurements there are two potential dividers given by Z_{eR} and R_{La} together with Z_{eT} and R_{Lb}, where R_{La} and R_{Lb} are amplifier input resistances required to bias the DC levels. This division must be smaller than the required measurement accuracy as the electrode impedances are variable and unknown.
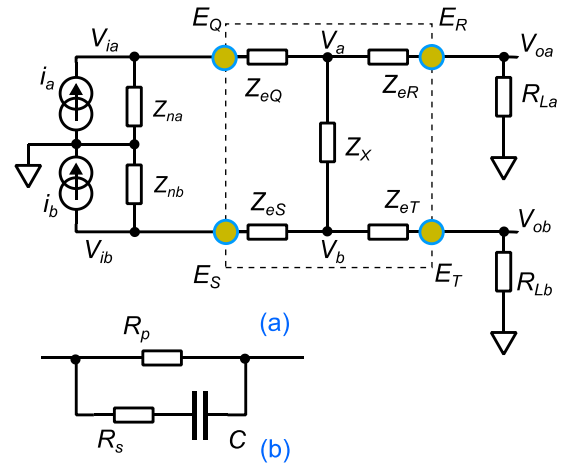
Fig. 1 a Model of current driven impedance spectroscopy system where Z_x represents the transfer impedance. The system is excited by a balanced drive current source, i_a and i_b, with the output voltage detected at V_{oa} and V_{ob}. The dotted line represents the volume of tissue under test including its transfer impedance, together with electrodes E_Q, E_R, E_S and E_T with their associated impedances Z_{eQ}, Z_{eR}, Z_{eS}, and Z_{eT}.
b Simplified Cole-Cole equivalent circuit used to model impedances

The approach of finding simplified equations for the system provides a useful guide for circuit design, revealing parameters to focus on for optimisation. However, it will not give precise

predictions of circuit behaviour especially at higher frequency where capacitive effects become more important and so if precise predictions of circuit behaviour were required, I would encourage the circuit designer to use a full Spice simulation.

The interactions between the instrumentation system and the electrode impedances set the limits for the current source Norton impedance, as well as the input impedances for voltage measurement. In addition, mismatches between the electrode impedance will cause other measurement artefacts and these are analysed by considering the full system common mode rejection ratio (CMRR).

C. Voltage mode excitation systems

Voltage driven systems are excited by a voltage source. In this type of system, the current applied is not directly controlled and is hence dependent on the impedance presented by the system under test. The applied current in a voltage driven system is dependent upon the system under test and care must be taken to ensure that the current does not exceed safety limits if the load impedance is too low. Alternatively if the impedance is too high the current could be too low and so the signal to noise maybe worse than required. In order to measure the transfer impedance the applied current must also be measured. In many medical systems, most of these problems may be overcome by using a voltage source with significant output impedance, as the current applied must be small to avoid undesired physiological effects and therefore the series impedance must be high. In some ways this blurs the distinction between voltage and current excitation systems. For the system developed in this paper we required a system where the injected currents were below sensory threshold. A threshold for sensitivity of 200 μA is given [30], and hence to give a reasonable head room the target for the applied current was set at 5 μA and the series resistance (R_{Ca} and R_{Cb}) was 100 kΩ. The analysis below assumes a similar series resistance. For consideration of the assumptions made in the following section it may be helpful to view sections V and VI which report impedance values of the order of 10 kΩ and 1 TΩ for the low frequency electrode and voltage channel input respectively.
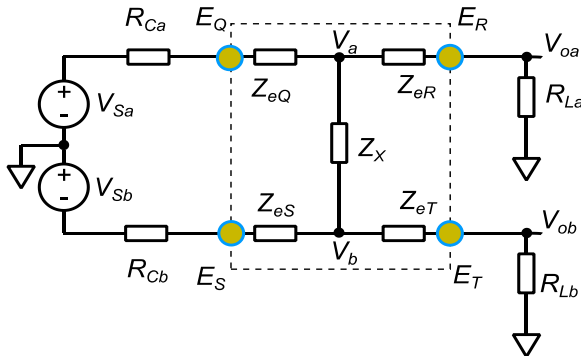

Fig. 2 Model of voltage driven impedance spectroscopy system. This system is excited by the balanced drive voltage source, V_{Sa} and V_{Sb}, with the output voltage detected at V_{oa} and V_{ob}.

Figure 2 displays a simplified circuit detailing the salient features of the voltage driven system front-end instrumentation, together with a model of the electrodes and the tissue under test. The differential voltage source V_{Sa} and V_{Sb}, source impedances R_{Ca} and R_{Cb} represent the voltage drive part of the system. Z_{eQ},

Z_{eR}, Z_{eS} and Z_{eT} model the electrode impedances and Z_x is the transfer impedance. The input load of the voltage measurement channel is given by R_{La} and R_{Lb}.

III. COMMON MODE

There are many mechanisms by which common mode voltages generate measurement artefacts. It is not sufficient to only consider the CMRR of the input buffer, as other sources of error will dominate. The largest errors in such systems emerge from interaction of the input impedance of the amplifiers and the electrode impedances. The electrode impedances are generally not well controlled and should be considered unknown; there are many forms of electrodes, however, all have to convert electronic conduction (within the metal wiring of the instrumentation) to ionic conduction (within the tissue being measured). This conversion requires ionization at the electrode surfaces and is critically dependent on the atomic makeup of the surface which leads to the effect of adding an unknown series impedance.

A. Development of an electrode mismatch error model for a voltage driven system

To estimate the common mode behaviour of the system we assume no differential signal, i.e. the transfer impedance Z_x is set to zero, so that $V_a = V_b = V_c$ and consequently the only signal present is the common mode voltage. For the voltage detection system to be insensitive to the electrode impedances, the input impedances of the voltage detection system must be very much greater than the electrode impedances. This assumption makes it more straightforward to estimate the common mode voltage, as we may ignore any current in Z_{eR} and Z_{eT}.

Looking at R_{Ca}, Z_{eQ}, Z_{eS}, R_{Cb} by using Kirchhoff's Voltage law and as we have set Z_x to zero hence we define $V_c = V_a = V_b$

$$V_c = -V_{Sb} + V_{R_{Cb}} + V_{Z_{eS}} \tag{1}$$

$V_{R_{Cb}} + V_{Z_{eS}}$ is part of a potential divider formed of $V_{R_{Ca}}$, $V_{Z_{eQ}}$, $V_{Z_{es}}$ and $V_{R_{Cb}}$

And therefore assuming a fully balanced drive $V_{Sa} = V_{Sb} = V_S$ and also assuming $R_{Ca} = R_{Cb} = R_C$ we may make the following approximation

$$V_{R_{Cb}} + V_{Z_{eS}} = 2 \cdot V_S \cdot \frac{R_{Cb} + Z_{eS}}{R_{Ca} + Z_{eQ} + R_{Cb} + Z_{eS}}$$

$$\approx 2 \cdot V_S \cdot \frac{R_c + Z_{eS}}{2R_c + Z_{eQ} + Z_{eS}} \tag{2}$$

Substituting (2) into (1) and assuming (Z_{eQ} and Z_{eS}) $<< R_C$

$$\frac{V_C}{V_S} = \frac{Z_{eS} - Z_{eQ}}{2R_c + Z_{eQ} + Z_{eS}} \approx \frac{Z_{eS} - Z_{eQ}}{2R_c} \tag{3}$$

Equation (3) gives the common mode voltage at the central node, V_C.

From this estimate of the common mode voltage, we may find the differential output voltage by assuming $R_{La} \approx R_{Lb} \approx R_L$:

$$V_{oa} = \frac{V_C \cdot R_L}{R_L + Z_{eR}} \tag{4}$$

$$V_{ob} = \frac{V_C \cdot R_L}{R_L + Z_{eT}} \tag{5}$$

The system detects the difference between V_{oa} and V_{ob}, and hence:

$$\frac{|V_{oa} - V_{ob}|}{V_C} = \left| \frac{R_L}{R_L + Z_{eR}} - \frac{R_L}{R_L + Z_{eT}} \right| \tag{6}$$

$$\frac{|V_{oa} - V_{ob}|}{V_C} = \left| \frac{R_L(Z_{eT} - Z_{eR})}{R_L^2 + R_L(Z_{eT} + Z_{eR}) + Z_{eT} \cdot Z_{eR}} \right| \tag{7}$$

Assuming $R_L \gg (Z_{eT}$ or $Z_{eR})$ the only significant denominator term is R_L^2 and hence simplifies to:

$$\frac{|V_{oa} - V_{ob}|}{V_C} \approx \left| \frac{Z_{eT} - Z_{eR}}{R_L} \right| \tag{8}$$

Combining (3) and (8) and assuming Z_{eR} and Z_{eT} are very much smaller than R_{Lb} to give:

$$\frac{|V_{oa} - V_{ob}|}{V_C} \approx \left| \frac{(Z_{eQ} - Z_{eS})(Z_{eR} - Z_{eT})}{2 \cdot R_L \cdot R_C} \right| \tag{9}$$

Examining Equation (9), if either the input or output electrode impedances (Z_{eQ} and Z_{eS}) or (Z_{eR} and Z_{eT}) are balanced then the error becomes zero. The error is inversely proportional to both R_C and R_L and therefore the error may be reduced by increasing the resistance of R_L. Apart from R_L, all other impedances are either not controlled by the designer or cannot be changed without adversely affecting the circuit behaviour because increasing R_C would reduce the applied current. A simple method to maintain the circuit D.C. bias levels, whilst dramatically increasing the effective value of the R_L resistors, would be to bootstrap these to the common mode voltage. Although not analysed in detail here, it is important that the two R_C resistors are matched, as their mismatch has a similar effect to a mismatch of the electrode impedances. The design shown below uses R_C set to 100 kΩ with a tolerance of 0.1 % (100 Ω) which is much less than the expected electrode impedance variation over the entire frequency range. This analysis does not include a model of the input capacitance of the amplifiers, which reduces the high frequency input impedance, however, this effect is offset to some extent by the fall with frequency of the electrode impedance (section VI).

B. Development of an electrode mismatch error model for a current driven system

Similar sources of measurement artefact exist for a current driven system but the exact source of error is a little different. A full description of the circuit behaviour was attempted with a symbolic mathematical package (wxmaxima) [26]; however, the number of terms in the describing equations became too large to successfully analyse the behaviour and so some simple approximations were required. If we assume that for a current drive system the Norton output impedance for the current sources is much higher than the electrode impedances, then the central point voltage is dominated by the mismatch in the source currents [16] and the loading impedance on the central point. The loading impedance is the parallel combination of the voltage detection system input impedances and Norton output impedance of the current sources. The Norton impedance of the current source will reduce with increase in frequency, again this is offset, to some extent, by the fall of electrode impedance with

frequency this is explored in greater detail by McEwan *et al.* [21].

The two current sources, to source and sink the current, are generally two separate Howland current source circuits. As they are two separate circuits, with currents dependent on several resistors, they will not be perfectly matched. The residual current due to this mismatch in the current sources, flows through the high input impedances of the voltage detection system. As this impedance is high it will generate a high voltage. If this voltage is too high, then any of the current sources, multiplexers or difference amplifiers may saturate. Even at lower voltages, there are similar CMRR problems to those in the voltage system described above. Sirtoli *et al.* [34] has developed a differential current source which will reduce current imbalance, however; the following analysis may be used in this case.

For the circuit in Figure 1, we will make a few assumptions to ease analysis. It is possible to use SPICE [17], for a fuller analysis, however, the system equations have the advantage of giving a much deeper insight into the circuit behaviour. Again we set Z_x to zero and then, as the following values are dependent on close tolerance components, we assume $Z_{na} \approx Z_{nb} = Z_n$ and $R_{La} = R_{Lb} = R_L$. We will define the current mismatch $(i_a - i_b) = \Delta i$ and then, assuming the electrode impedances are much smaller than Z_n and R_L, the common mode voltage V_C may be approximated by the difference current multiplied by the parallel combination of the two Norton and load impedances Z_n and R_L respectively.

$$V_C \approx \Delta i \frac{Z_n \cdot R_L}{2(Z_n + R_L)} \tag{10}$$

As above find the differential output from this common mode signal acting on the combination of the electrode impedances and load resistance by substituting V_C from (10) into (8)

$$\frac{|V_{oa} - V_{oa}|}{\Delta i} \approx \frac{Z_n}{2(Z_n + R_L)} \cdot |Z_{eT} - Z_{eR}| \tag{11}$$

Equation (11) shows that, for the current driven system, artefacts are dependent on the difference between the electrode impedances Z_{eT} and Z_{eR} and current source mismatch. In addition, increasing the Norton (Z_n) impedance does not reduce artefact due to electrode mismatch. As Z_{eT} and Z_{eR} may be significantly greater than the transfer impedance to be measured, the balance of the current drives is critical; therefore, some form of active balancing may be helpful [18]. Unlike the voltage driven system increasing R_L has the side effect of increasing the common mode voltage, which may lead to saturation in the current drive or voltage detection systems. The use of bootstrapping described below will make the assumption made by Langlois *et al.* [32] valid that the input impedance of the voltage measurement channel is high enough to be ignored.

IV. DESCRIPTION OF A CIRCUIT BASED ON THE VOLTAGE DRIVEN PRINCIPLE

Most electrical impedance spectroscopy and electrical impedance tomography systems require some method to multiplex the electrodes to the drive and voltage detection systems, with this multiplexer inevitably adding parasitic impedance to the electrodes. In addition, the electrodes require wiring to instrumentation, which adds further parasitic capacitance. Oh *et al.* [19] describes a current source type

system with some similarities to our voltage drive system, however the voltage drive system makes it much easier to fully account for variation in electrodes and control parasitic effects. Referring to Figure 2, the transfer impedance, Z_x, is typically much smaller than the electrode impedances Z_{eQ}, Z_{eR}, Z_{eS} and Z_{eT} thus the voltage between electrodes E_Q and E_S is much greater than the voltage across Z_x, and hence the voltage between E_R and E_T. Therefore, the measured voltage is very sensitive to any coupling between electrodes E_Q and E_R or E_S and E_T within the wiring or through any parasitic impedance within the multiplexers.

In our novel system, all of the electrodes are buffered by a very high input impedance buffer, which may be placed physically close to the electrodes to dramatically reduce the sensitivity to the parasitic currents within the wiring and multiplexer systems. As buffering may be local to the electrodes, there is no requirement for routing the high impedance signals from the electrodes to the central instrumentation. There are several additional advantages of buffering the voltage of all the electrodes, including:

- Easy wiring of the electrodes to the main instrumentation with simple screened cable
- No wiring of high impedance signals required between the current source and electrodes
- Buffered electrode potential available is for monitoring the electrode side of the Thévenin resistor (Fig.4 R2 and R5)
- Buffered electrode potentials are available for other physiological measurements such as EEG, EMG, ECG etc.

Tozer [29] described active electrodes to increase the electrode input impedance for magnetic induced impedance imaging systems and they have also been employed for EIT systems [27][31]. For current driven systems the current source is usually implemented centrally and hence the current source output will be shunted by the cabling capacitance. As the system described here only requires a resistor for driving the current, it is easy to create fully active electrodes where all the wiring after the electrodes is low impedance. By directly measuring the current by relaying the measurement through a similar channel to that of the voltage measurement system phase shift errors will be reduced. Thus phase compensation described in [33] will be alleviated because there will be good phase match between the voltage and current measurement channels.

V. HIGH INPUT IMPEDANCE UNITY GAIN VOLTAGE BUFFER

A very high input impedance buffer is constructed using the MAX44260 (U1), as shown schematically in Figure 3.a. This amplifier is a CMOS op-amp with a low input capacitance of 0.4 pF. One of the requirements of the medical safety standard BS EN IEC 60601 is that a medical device shall be single fault safe, and as an amplifier fault could apply DC to the patient, the amplifier is capacitively coupled to the electrodes. The DC operating point is set by two 20 MΩ resistors (R4 and R5) and the effective loading to the electrode is reduced significantly below that implied by 20 MΩ by bootstrapping the midpoint. This is achieved by connecting the midpoint to the buffer output via R3. At low frequencies, the input impedance (Figure 3.c) is

dominated by the bootstrapped bias resistance, whereas at higher frequencies, the input impedance is dominated by the op-amp input capacitance. The input impedance of this circuit was modelled using LTSpice [20] over the full frequency range. Maxim publish a SPICE subcircuit model of the MAX44260, however, this subcircuit includes modelling of the power supply enable circuit, which causes problems in finding the DC operating point for the SPICE AC analysis. The subcircuit also includes the inner model (MAX44260A), which models the amplifier itself and was used to model the circuit behaviour.
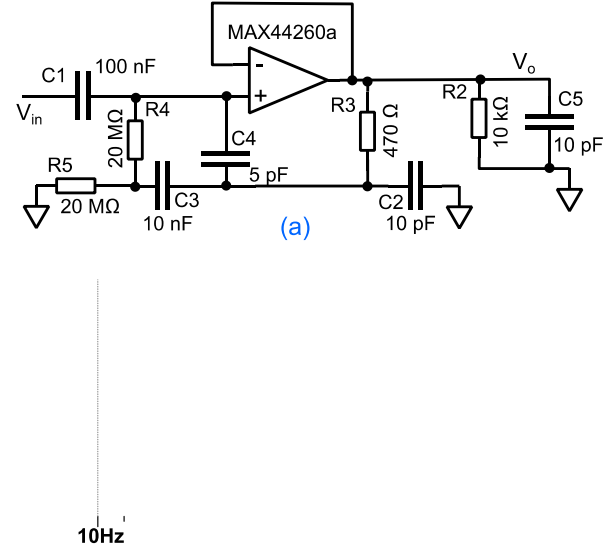

Fig. 3 SPICE model and results for high input impedance buffers, a = buffer circuit; b = voltage gain and phase; and c = input impedance. R2 and C5 model likely load impedance when the circuit is directly connected to a multiplexer. C2 and C4 model likely circuit board capacitances.

The buffer has a -3 dB bandwidth over the range 40 mHz to 15 MHz. The gain of the system (Figure 3.b) is flat within 1:10000 over the frequency range, from 50 Hz up to about 20 kHz, and over 1:400 up to 1 MHz. Op-amp data sheets usually do not give enough information to estimate the likely variations in these gain values; however, even if there were significant variation compared to these values, the intra op-amp gain variation would have a minor effect on the overall system CMRR. The input impedance, as given by the input voltage / input current, is equivalent to an input impedance of a pure capacitance of 0.4 pF over most of the frequency range (100 Hz to 1 MHz). Below 100 Hz the impedances are extremely high, dependent on the interaction of R5 and C3. To make the spice

model as accurate as possible, circuit board layout capacitances C2 and C5 have been included together with R2 the input resistance of the following buffer.

A description of the full system follows, as displayed schematically in Figure 4. The differential buffer, U7 (THS4531), applies a signal to R2 and R5 via the crosspoint switch U1 (ADG2188) where the switches are closed at locations A and B. The drive signal is also connected to the four input subtractor, U8.
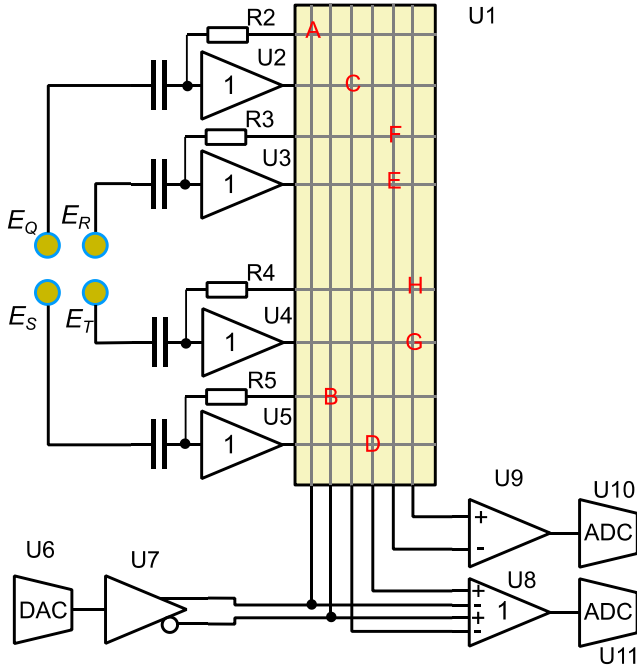

Fig. 4 Schematic diagram of full EIS system including the crosspoint switch (U1). U10 digitises the voltage channel and U12 digitises the current channel. The letters indicate a typical configuration for the switch settings

Fully differential op-amps of the type THS4531 are useful for generating differential drive signals due to their very closely matched differential outputs (-65 dB at 1 MHz), and their independence to resistor tolerances. U2, U3, U4 and U5 are the high impedance buffers, described in section V. U2 and U5 relay the potential on the electrode side of the two Thévenin resistors (R2 and R5) back via the crosspoint switch connection C and D to U8. Thus, the output of U8 is given as V(R2) – V(R5) or 2 * R2 * I, where I is the applied current. U8 and U9 were implemented utilising the THS4531 op-amp whose differential output was used to drive differential input ADCs. The voltages on electrodes E_R and E_T are relayed by U3 and U4 to the voltage measurement channel U9 by the crosspoint switch connections E and G. By closing connection F and H, the output of the bufferes U3 and U4 is applied to R3 and R4 and hence, an almost identical voltage appears on both sides of resistors R3 and R4. This bootstrapping reduces any current that would otherwise flow through resistors R3 and R4 into parasitic capacitances in the crosspoint switch and, hence, minimizes the possible loading of the electrodes.

A full description of the 3D limb system would be outside the scope of this paper but for completeness a list of system components follows. The signal was generated by an AD9838 dds device clocked at 10 MHz. Voltage and current channel signals are digitised by AD9251 ADC. The signals are

demodulated, within the stm32f746 microcontroller, by multiplying by a digitally synthesized version of the sinusoidal and cosinusoidal version of the dds waveforms.

VI. Electrode measurements

The 3D limb EIS system uses 7 mm diameter gold electrodes and it would be very useful to know what the probable electrode mismatch is likely to be, however we do not have access to a large number of electrodes to obtain a statistically useful number of measurements [35]. To provide some design data we used another electrode system where we do have access to a large number of measurements (n = 409). These are 0.6 mm silver / silver chloride electrodes, whereas the system proposed here uses 7 mm gold electrodes, obviously these electrode systems are very different but this section is included to give a qualitative feel for the variation that may be present in electrode systems. A single measurement from a 7 mm gold electrode yielded an impedance of about 1/10 that of the 0.6 mm electrodes and this seems to be reasonable as the area of the gold is about 100 times that of the smaller electrodes but generally gold is a less effective electrode with higher impedances. The contact impedance has two main elements; that of the electrode itself and that due to tissue spreading. The aim of the electrode measurement work was to identify the impedance of the electrode itself rather than the spreading resistance and so we used saline with a physiologically high conductivity of 1.2 S/m [23]. The method described in [6] was used to estimate the spreading resistance for the 0.6 mm electrodes for a large tank, providing a value of approximately 700 Ω. Some measurements at high frequency are smaller than 700 Ω; the cause of the inconsistency is yet to be conclusively investigated, but it is likely due to the capacitive effects that make the electrode area effectively larger at higher frequency. Measurements were made using a Solartron impedance analyser model SI 1260, where one terminal pair was connected to the electrode under test and the other to a much larger (2 cm x 3 cm) silver / silver chloride return electrode. For the purposes of making a simple model for simulation work, an iterative approach was used to estimate the parameters for a simplified Cole-Cole circuit, as in Figure 1.b, tabulated in Table 1. As these measurements are taken from electrodes used for EIS measurements, they provide a realistic model that may be used for simulation and to model the magnitude and variance of electrode impedances.

Table 1 Equivalent circuit model parameters for the extreme cases of electrode impedances

Model	Rs (Ω)	Rp (Ω)	C (nF)
2.5 %	300	3000	750
Median	550	8000	250
97.5 %	700	16000	150

VII. Spice model of the circuit

A model of the front-end circuit was constructed using the LTspice simulator; a hierarchical approach has been taken to simplify the schematic diagrams. The top level schematic is provided in Figure 5.a, the two sources, Vsa and Vsb, are two antiphase voltage sources that drive current through the two 100 kΩ resistors (R2 to R5) within the buffer sub circuits X8

and X9 and are shown in detail in Figure 5.b. These buffer circuits facilitate measurement of the voltage appearing on the electrodes with minimal extra loading. This arrangement allows for direct measurement of the voltage across the Thévenin resistors (X9.R and X8.R) and, hence, the current. For simulation, the two voltage dependent voltage sources E1 and E2 model a perfect subtraction process and so their output is a measure of the injected current. The LTspice waveform display,
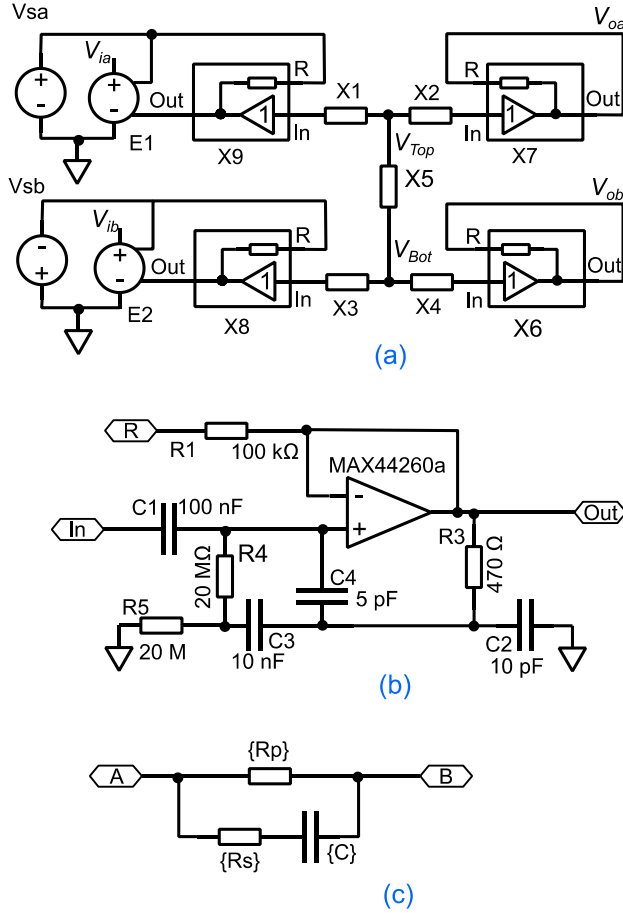

(a)

(b)

(c)

Fig. 5 a Hierarchical spice model of whole system with buffer component shown in b and Cole-Cole model for the impedance under test and electrode impedances shown c

which allows for processing using mathematical functions, was utilized to display the measured voltage divided by the average source and sink currents and the waveform of measured impedance. The electrodes were modelled by the sub-circuits X1 through to X4, with X5 modelling the transfer impedance under test. The output voltage is buffered by X6 and X7.

The first test was with a very low transfer impedance of 1 Ω, selected as additive artefacts are easiest to detect under these conditions. The waveform display was used to simulate the detection system, which may be configured to show both the transfer impedance directly in green (V(top)-V(bot))/Ix(x5:B) and the output of the system in red 100k*(V(voa)-V(vob))/((V(ia)-V(ib))/2). The results shown in Figure 6 were generated with electrode impedances set to their maximum (97.5 %) values, as tabulated in Table 1. The artefact error is within 4 m·Ω over the full bandwidth of 10 Hz to 600 kHz. The phase error is almost identical to that shown in Figure 3 and is mainly due to the buffer amplifiers and as it is not dependent on

the electrodes/transfer impedance it could easily be calibrated out. For Figure 6.b and 6.c, the electrodes are set to the corner case of the extreme impedances, where X1 and X2 are set to the minimum value and X3 and X4 are set to the maximum value in which case there is an increased error of about 80 mΩ. Another source of mismatch is the variation of the coupling capacitances, however, modelling a drop of 10% (from 100 nF to 90 nF) the artefact changed from 9 mΩ to 9.1 mΩ at 76 Hz, the lowest operational frequency for our system. This result provides reassurance that the lower frequency cut off of 40 mHz is sufficiently low that carful matching of the coupling capacitances (fig 5b C1) is not required. When the test impedance was set to a larger value of Rs=66.6 Ω, Rp=200 Ω, C=1000 nF, it can be seen that there is very little gain type error, excepting a small phase shift at the highest frequencies.

(a)

(b)

(c)
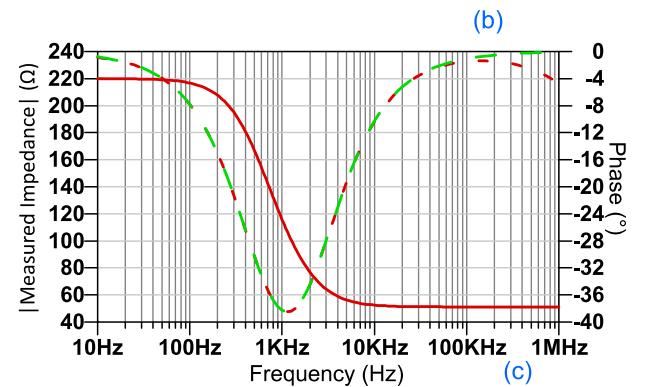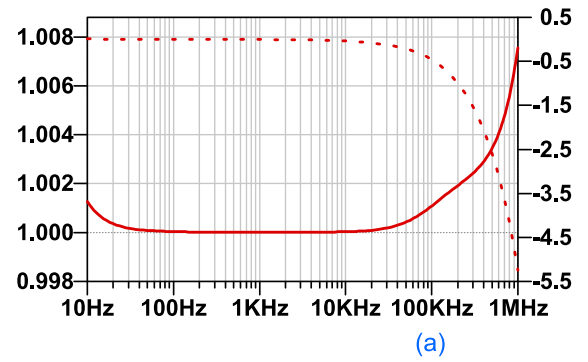
Fig. 6 LTspice model results. Green curves are the impedances of the test network and the red curves are the output of the circuit. Both impedance magnitude and phase are plotted.
a and b simulation with 1 Ω test impedance, c Cole-Cole physiological impedance model with value set at 220 Ω, 67 Ω and 1 nF for Rp, Rs and C respectively. Electrode impedance set to the upper limit values for a. For, b and c electrode impedance set to the unbalanced values from table 1.

VIII. Experimental Measurements of EIS System Performance Against Test Networks

The 3D limb EIS device incorporated the front-end instrumentation described in this paper and forms part of a clinical instrument, which is designed to take measurements from human tissue involving skeletal muscle. A detailed description of the full system is beyond the scope of this paper; however, in brief, this device has two sets of eight electrodes held in two opposing parallel plates. The distance between the two plates may be adjusted such that it makes contact with both sides of a body part, such as the forearm. Each of the plates holds two rows of 7 mm diameter gold electrodes on 15 mm centres with 30 mm between the centres of the two rows. The front-end electronic instrumentation is as described in this paper. An ARM STM32F746 microcontroller was employed for system control in addition to signal generation and detection, wirelessly linked to a PC to record data.

To explore the performance of the circuit in the presence of electrode mismatch, the test circuit provided in Figure 7a was used. This test circuit modelled the likely extremes for electrode impedances, as found for the 0.6 mm diameter Zilico electrodes using the models developed above. The Zilico electrodes are quite different from the large electrodes used for the 3D limb device, however, this device is intended to contact keratinized skin, and the spreading impedance of this tissue will, partially, offset the difference in area. It would be useful to gather data on the impedance of the larger electrodes, in order to better quantify the likely artefacts attributable to electrode mismatch. The system was configured to take four measurements from each configuration with the drive and voltage sensing electrodes swapped. Figure 7.b shows the results of these tests with through hole resistors of 10 kΩ, 1 kΩ, 100 Ω, 10 Ω and 1 Ω, on a logarithmically scaled y-axis so that these may be displayed alongside one another. For the larger test impedances, the curves sit very close to expected values. All the spectra are flat, displaying values close to the test impedance. At the highest impedances there is almost no low frequency roll off as observed by McEwan *et al.* [21]. This is due to the extremely high input impedance achieved by the bootstrapping of the input amplifiers. As the electrode mismatch generally causes additive artefact errors at high impedances, there is very little significant artefact. Whereas, at lower impedances the artefact becomes more apparent, it equates to an error in the order of 1 Ω. It is possible to observe the limits of the dynamic range of the system; this is where the noise floor becomes apparent at the lower impedance curves. For the 1 Ω test impedance, system noise is more obvious and by consideration of this noise and artefact, a system dynamic range is estimated to be over 80 dB. Figure 7c shows phase normalised by subtracting the average phase shift for the three middle test resistances. The reduced signal to noise for the 1 Ω test impedance makes phase measurements noisy and was not plotted. Up to a test impedance of 1 kΩ there is only a very small phase lag at the highest frequency of less than 3 ° and 16 ° for 10 kΩ. For the 1 Ω test resistance it is possible that parasitic inductance will make a small contribution to the observed phase shift. The system has a phase shift due to difference in the voltage and current channels and figure 7c plots phase normalised by

subtracting average phase shifts measured from 1 kΩ, 100 Ω, 10 Ω resistors.
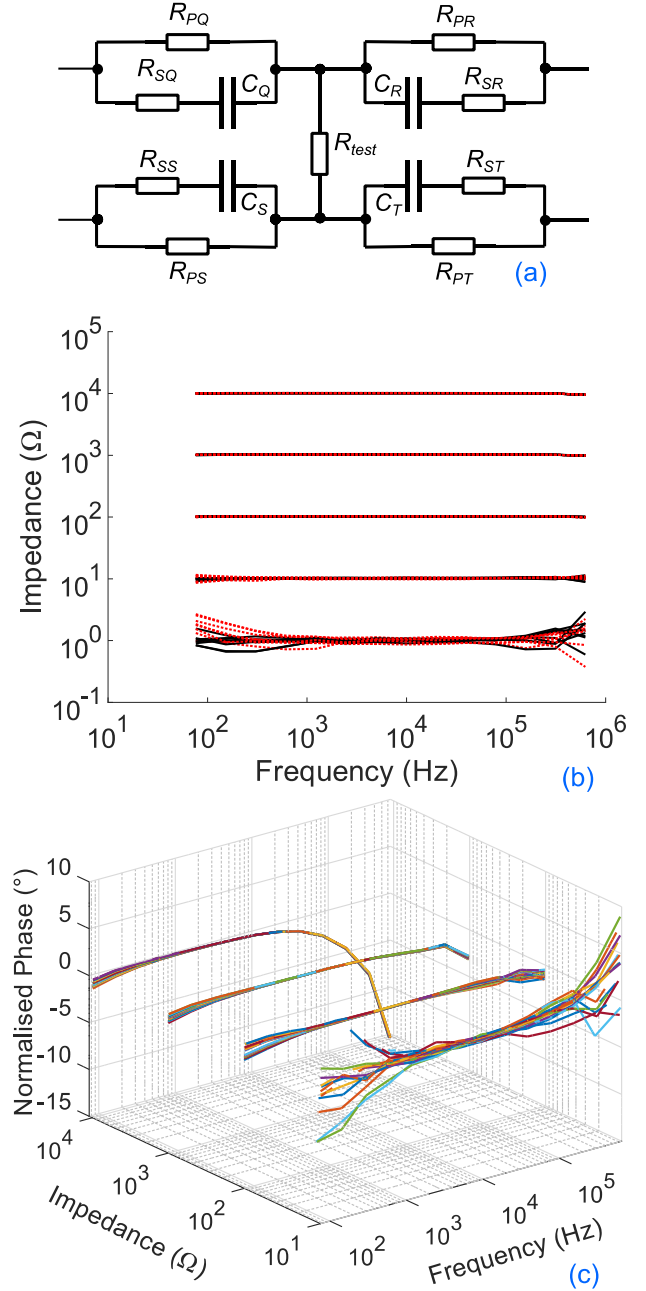

Fig. 7 Experimental measurements made against test networks using the build system. a Test circuit with electrode impedance models using mismatched values taken from the extremes tabulated in table 1.
b. The effects of mismatching electrode impedance models. There are 5 groups of curves corresponding to test impedance of 10 kΩ, 1 kΩ, 100 Ω, 10 Ω and 1 Ω. c. The same as b. but also showing normalized phase. Two electrode impedances were set to the minimum extreme and two set to the maximum extreme and each of the 16 curves in each group show different permutations of these two. The red dashed curves are where the voltage drive and therefore voltage receive are mismatched and the black curves are

The main gain stage for the system employed THS4531 fully differential amplifiers, which have a respectable input noise of 10 nVHz$^{-\frac{1}{2}}$; however, as this device requires a circuit with a

relatively low input impedance, it is far from ideal. Lower noise and better CMRR could probably be achieved with a circuit as outlined by Analog Devices [22].

IX. SALINE MEASUREMENTS

Saline measurements are useful for a number of reasons. Firstly, they give a good indication as to whether or not the device functions correctly in a controlled environment; the device may be held in a bath containing a saline solution whose conductivity can be measured directly with a conductivity meter. Secondly, for impedance spectroscopy device measurements to be transferable, their measurements should be calibrated to SI unit systems. As resistivity is related to transfer impedance by the cell constant, the transfer impedance may be multiplied by the cell constant to give resistivity. However, due to the heterogeneous nature of body tissue, resistivity measurements will not be directly comparable to the published data for tissue resistivity.
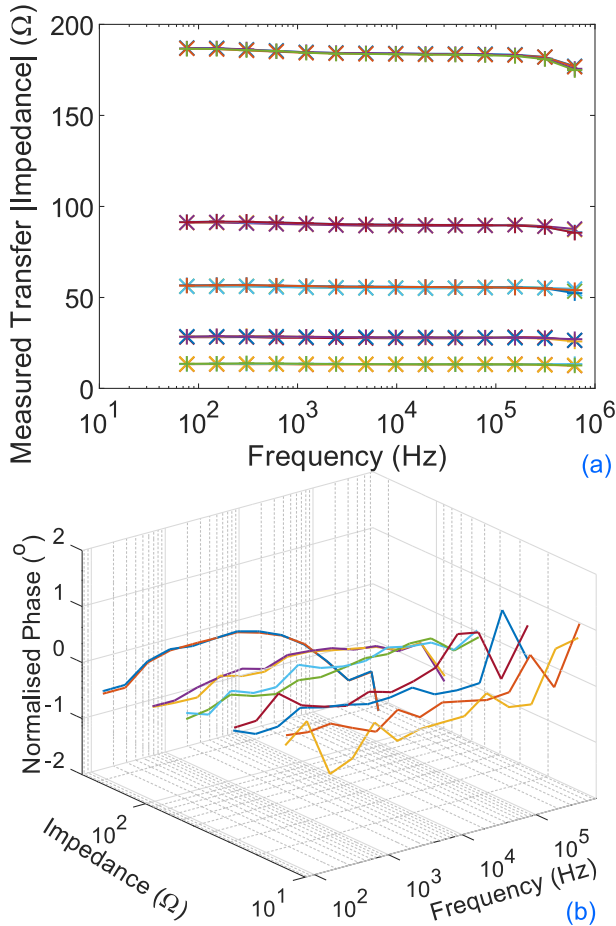

(a)

(b)

Fig. 8a Spectra measured from the four electrodes, each 7 mm diameter, in a linear arrangement with 15 mm between the electrode centers. Five solutions with respective resistivities of (15.6, 8.28, 4.97, 2.48 and 1.27) Ω·m were used. Each measurement set was repeated twice, with measurements made with the voltage drive on the inner electrode pair, and voltage detected on the outer pair, then swapped to generate a reciprocity pair. b including normalized phase

The 3D Limb device was placed, along with the top plate, in a shallow saline bath (1 cm deep) and the instrument was configured to make impedance measurements from four electrodes in a linear arrangement. The conductivity of the saline was adjusted to convert a likely physiological range [23] of resistivities (15.6 to 1.27) Ω·m and the results are plotted in Figure 8. As would be expected over this frequency range, all the transfer impedances are almost totally independent of frequency [24]. There is a small roll-off at the highest frequency at the highest resistivity (15.6 Ω·m), which is likely to be due to the interaction between the electrode impedances and the input capacitances of the circuit. The advantage of this circuit is that the channels are buffered before any multiplexing and hence these capacitances are very low, producing the resultant flat spectra. The role off can be seen more clearly in the phase plotted in figure 8b, which plots the phase normalised with the same values as found in section VIII.

The cell constant may be found by plotting the solution conductivity against measured transfer impedance; the cell constant is the gradient of the least square line of best fit. The test solutions were made by adding sodium chloride to water, with conductivity directly measured with an Orion Star™ A322 conductivity meter. A titration method was employed to make up solutions in the required conductivity ranges. For the limb device, the results are displayed in Figure 9. Two data sets were plotted, '+' with the electrodes in a linear arrangement with 15 mm between electrode centres, and, 'x' a square arrangement with 30 mm between electrode centres. For these two simplistic electrode arrangements the cell constants were found to be 18.98 m^{-1} and 9.97 m^{-1}, respectively at the mid range frequency of 2441 Hz.
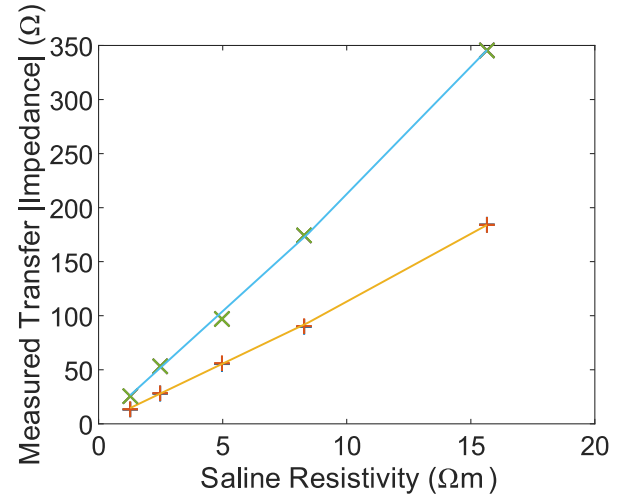

Fig. 9 Cell constants found for two cell geometries one linear ('x') and the other with in a square arrangement ('+') and the frequency of 2441 Hz. The straight lines are linear least square fit lines with respective gradients (and therefore, cell constants) of (18.98 and 9.97) m^{-1}.
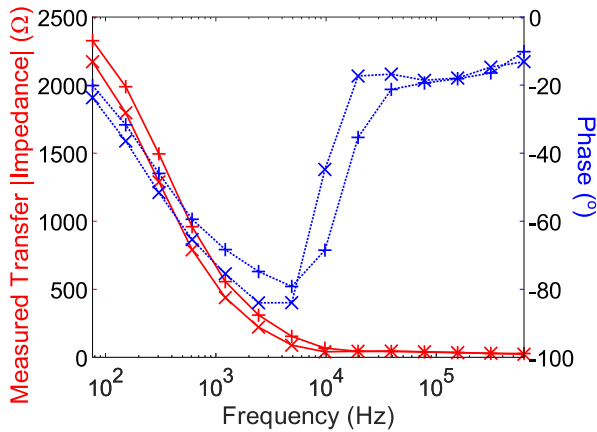
Fig. 10 Typical impedance measurement from a human subject with electrodes in a linear arrangement over the forearm flexor muscles. The two lines show the reciprocity pair [25] with the 'X' reflecting the drive on the inner electrodes and the '+' the drive on the outer electrodes. The phase has been normalised by subtracting a spectra recorded from a 100 Ω resistor

X. Measured spectrum from human subjects

The 3D Limb device is now in use as part of a clinical trial investigating EIS utility for assessing muscle health. Figure 10 shows typical measurements taken from a human forearm. The two curves show the effects of transposing the drive and receive electrodes. Reciprocity theory [25] predicts symmetry so that swapping drive and receive will produce identical spectra, however this will not include artefact generated by electrodes, hence plotting the two curves gives a good indication of the system artefacts. As these two curves lie close to each other this gives confidence that the artefacts are small.

XI. Conclusions

This paper demonstrates that by making some simple assumptions it is possible to analyse the effects of unbalanced electrode impedances for a wide range of impedance spectroscopy devices, which would otherwise result in significant measurement artefacts. The simplified equations developed over the course of this paper provide insight into the circuit parameters dominating the artefacts, chiefly voltage channel input impedance. Using this insight, novel circuit architecture has been developed that reduces these artefacts by increasing the circuit's input impedance. By minimising connections to the input nodes and bootstrapping all bias networks, input impedances greater than 1 GΩ, in parallel with 0.4 pF, were achieved for a system that meets the regulatory standards for isolation by full capacitor coupling. This architecture has been tested with a full circuit simulation and in physical hardware under a range of conditions. Hardware performance was tested against test circuits with typical mismatched electrode impedances, within saline water baths, in addition to measurements from a human subject. The results are promising; showing a practical application of the theory, enabling the reduction in artefact in measurements made using EIS, and an *in vivo* study has just begun investigating EIS for a biomarker for conditions involving human skeletal muscles.

References

[1] J.A. Tidy, B.H. Brown, T.J. Healey, S. Daayana, M. Martin, W. Pendiville, and H.C. Kitchener, "Accuracy of detection of high-grade cervical intraepithelial neoplasia using electrical impedance spectroscopy with colposcopy," BJOG Mar 2013, 120(4):pp 400-411 DOI: 10.1111/1471-0528.12096

[2] J.J.P. Alix, H.E. McDonough, B. Sonbas, S.J. French. D.G. Rao, V. Kadirkamanathan, C.J. McDermott, T.J. Healey, and P.J. Shaw, "Multi-dimensional electrical impedance myography of the tongue as a potential biomarker for amyotrophic lateral sclerosis," Clin Neurophysiol. Apr 2020, 131(4):pp 799-808 DOI: 10.1016/j.clinph.2019.12.418.

[3] P. Metherall, D.C. Barber, R.H. Smallwood, and B.H. Brown. "Three-dimensional electrical impedance tomography" Nature Apr 1996; 380; pp 509-512 DOI: 10.1038/380509a0

[4] A. McEwan, A. Romsauerova1, R. Yerworth, L. Horesh, R. Bayford and D. Holder, "Design and calibration of a compact multi-frequency EIT system for acute stroke imaging," Physiol. Meas. 27 (2006) S199–S210 doi:10.1088/0967-3334/27/5/S17

[5] J.Avery, T. Dowrick, M. Faulkner, N. Goren and D. Holder, "A Versatile and Reproducible Multi-Frequency Electrical Impedance Tomography System," Sensors 2017, 17, 280; DOI:10.3390/s17020280

[6] M. W. Denhoff, "An accurate calculation of spreading resistance," J. Phys. D: Appl Phys. Apr 2006; 39(9); p 1761

[7] S. Grimnes, and O. G. Martinsen, "Sources of error in tetrapolar impedance measurements on biomaterials and other ionic conductors," J. Phys. D: Appl. Phys. 2006 40(1): p 9.

[8] P. Kassanos, F. Seichepine, and G-Z. Yang, "A Comparison of Front-End Amplifiers for Tetrapolar Bioimpedance Measurements," IEEE Trans. on Instrumentation and Measurement. 2021; 40; pp 1 - 14

[9] B. Fu, and T. J. Freeborn, "Residual impedance effect on emulated bioimpedance measurements using Keysight E4990A precision impedance analyzer," Measurement. Feb 2019; 134; pp 468 – 479 DOI: 10.1016/j.measurement.2018.10.080.

[10] J.M. Torrents, and R. Pallas-Areny, "Compensation of Impedance Meters When Using an External Front-End Amplifier," IEEE Transactions on Instrumentation and Measurement. Apr 2002; 51(2); pp 310 – 313.

[11] M. Rahal, J.M. Khor, A. Demosthenous, A. Tizzard, and R. Brayford, "A comparison study of electrodes for neonate electrical impedance tomography," Physiol. Meas. Jun 2009; 30(6); pp 73-74. DOI: 10.1088/0967-3334/30/6/S05.

[12] "Medical electrical equipment Part 1: General requirements for basic safety and essential performance" BS EN 60601-1:2006+A12:2014, ISBN 978 0 539 00575 2

[13] H. Wi, H. Sohal, A.L. McEwan, E.J. Woo, and T.I. Oh, "Multi-Frequency Electrical Impedance Tomography System With Automatic Self-Calibration for Long-Term Monitoring," IEEE Trans. on Biomedical Circuits and Systems. Feb 2014; 8(1); pp 119 – 128. DOI: 10.1109/TBCAS.2013.2256785

[14] C.I. Trainito, O. Francais, and B. Le Piouffle, "Analysis of pulsed electric field effects on cellular tissue with Cole–Cole

model: Monitoring permeabilization under inhomogeneous electrical field with bioimpedance parameter variations," Innovative Food Science & Emerging Technologies, May 2015; 29: pp 193 – 200. DOI: 10.1016/j.ifset.2015.02.004

[15] Texas Instruments Incorporated, "Ultra Low Power, Rail-to-RailOutput, Fully-Differential Amplifier," SLOS358C–SEPTEMBER 2011 –REVISED APRIL 2020 [Online]. Available:
https://www.ti.com/product/THS4531?qgpn=ths4531.
[Accessed: 29- Mar- 2021]

[16] P. Bertemes-Filho*, A. Felipe, V. C. Vincence, "High Accurate Howland Current Source: Output Constraints Analysis," Circuits and Systems, 2013, 4, 451-458 DOI: 10.4236/cs.2013.47059

[17] L.W. Nagel, and D.O. Pederson, *SPICE (Simulation Program with Integrated Circuit Emphasis)*, Memorandum No. ERL-M382, University of California, Berkeley, Apr. 1973

[18] J. Rosel, and P. Riu, "Common-mode feedback in electrical impedance tomography," Clin. Phys. Physiol. Meas. 1992; Suppl A: pp11-14 DOI: 10.1088/0143-0815/13/a/002.

[19] T.I. Oh, E.J. Woo, and D. Holder, "Multi-frequency EIT system with radially symmetric architecture: KHU Mark1," Physiol. Meas. Jul 2007; 28(7); pp 183 – 196. DOI: 10.1088/0967-3334/28/7/S14.

[20] "LTspice | Design Center | Analog Devices", Analog.com, 2021. [Online]. Available: https://www.analog.com/en/design-center/design-tools-and-calculators/ltspice-simulator.html. [Accessed: 30- Mar- 2021].

[21] A. McEwan, G. Cusick and D. S. Holder, "A review of errors in multi-frequency EIT instrumentation," Physiol. Meas. 28 (2007) S197–S215 doi:10.1088/0967-3334/28/7/S15

[22] R. Juszkiewicz, "A New Spin on a Classic Architecture: Achieving a Fully Differential Output Using Single-Ended Instrumentation Amplifiers | Analog Devices," Analog.com, 2019. [Online]. Available: https://www.analog.com/en/analog-dialogue/raqs/raq-issue-161.html. [Accessed: 30- Mar- 2021].

[23] Itis.swiss. 2021. *Dielectric Properties » IT'IS Foundation*. [online] Available at: <https://itis.swiss/virtual-population/tissue-properties/database/dielectric-properties> [Accessed 30 March 2021].

[24] R. Sauerheber and B. Heinz, "Temperature Effects on Conductivity of Seawater and Physiologic Saline, Mechanism and Significance," Chem. Sci. J, 2015; 6: pp 4 – 9. DOI: 10.4172/2150-3494.1000109

[25] J. Malmivuo, "Application of the principle of reciprocity to impedance tomography and other problems in bioelectromagnetism," 2010 12th Biennial Baltic Electronics Conference, Tallin, Estonia; pp 61 – 64. DOI: 10.1109/BEC.2010.5630918.

[26] wxMaxima, Version 19.01.2x, http://wxmaxima-developers.github.io/wxmaxima/

[27] T. Zagar and D. Krizaj, "An instrumentation amplifier as a front-end for a four-electrode bioimpedance measurement," 2007 Physiol. Meas. 28 N57

[28] Y. Wu, D. Jiang, A. Bardill, R. Bayford and A. Demosthenous, "A High Frame Rate Wearable EIT System Using Active Electrode ASICs for Lung Respiration and Heart Rate Monitoring," IEEE Trans.

Circuits and Systems–I, Vol. 65, No. 11, November 2018

[29] R. C. Tozer, "A low input capacitance sense amplifier for impedance imaging applications," 1992 Meas. Sci. Technol. 3 508

[30] J. Patrick Reilly, "Applied Bioelectricity," Springer-Verlag new York, 1998, Table 7.6, ISBN 0-387-98407

[31] P. O. Gaggero, A. Adler, J. Brunnerand P. Seitz, "Electrical impedance tomography system based on active electrodes," Physiol. Meas. 33 (2012) 831–847

[32] P. J. Langlois *et al.*, "On the application of frequency selective common mode feedback for multifrequency EIT," 2015 Physiol. Meas.36 1337

[33] P. Kassanos and Guang-Zhong Yang, "A CMOS Programmable Phase Shifter for Compensating Synchronous Detection Bioimpedance Systems," 2017 24th IEEE International Conference on Electronics, Circuits and Systems (ICECS), 2017-12, Vol.2018-, p.218-221

[34] V. Sirtoli, K. Morcelles, J. Gomez and P. Bertemes-Filho, "Design and Evaluation of an Electrical Bioimpedance Device Based on DIBS for Myography during Isotonic Exercises," J. Low Power Electron. Appl. 2018, 8(4), 50

[35] Zilico private commination

T. Jamie Healey was born in Chester, United Kingdom. He graduated with a BEng.(Hons) in electronic engineering and a PhD in medical physics, in 1989 and 1995 respectively, both from the University of Sheffield. He is a Clinical Scientist working in the Medical Device Innovation group in the Department of Clinical Engineering at Sheffield Teaching Hospitals NHS Foundation Trust.

His clinical interests include ophthalmic electrophysiology. Currently he is working of projects in EIS and a large NIHR Invention for Innovation (i4i) Programme project developing an array-based electrical stimulation system to deliver sensory barrage stimulation for post stroke therapy to alleviate spasticity. He has over 24 publications in peer-reviewed journals and holds 2 patents.

Dr Emily Rose Billinge is currently a final year trainee clinical scientist specialising in ophthalmic electrophysiology at Sheffield Teaching Hospitals NHS FT, where she also assists in providing an Electrodiagnosis module to second year orthoptics students for the University of Sheffield. Prior to this, she graduated in 2012 with a BSc (Hons) in Neuroscience with Pharmacology, and in 2015 with a PhD in Analytical Chemistry from Loughborough University, developing proof-of-concept biomarker assays utilising superparamagnetic nanoparticles, aptamers, and resistive pulse sensing technologies. Following her PhD, she worked as a post-doctoral research technician in the Stem Cell Research and Advanced Bioengineering Lab (SCRABEL) of Canterbury Christ Church University.

Dr Alix is a clinician scientist working across the preclinical and clinical divide to develop and test novel biomarkers of neurological diseases. He received degrees in basic neuroscience (BSc and PhD) and medicine from the University of Leicester Medical School MB/PhD programme. He then undertook combined academic and clinical training at Imperial College, London and the University of Sheffield, gaining membership of the Royal College of Physicians. He has a

particular interest in applying impedance spectroscopy to disorders of nerves and muscles and was awarded the 2017 Lord Adrian Prize by the British Society for Clinical Neurophysiology for his work trialling a novel impedance spectroscopy device in motor neurone disease. He is a practising consultant clinical neurophysiologist working within a regional clinical neuroscience centre.

Visakan Kadirkamanathan (M'1991) was born in Jaffna, Sri Lanka. He graduated with a B.A (Hons) in electrical and information sciences and a Ph.D. in information engineering, in 1987 and 1992 respectively, both from the University of Cambridge, UK.

He is Professor of Signal and Information Processing at the Department of Automatic Control and Systems Engineering and is also the Director of the Rolls-Royce supported University Technology Centre in Control, Monitoring and Systems Engineering at the University of Sheffield, UK. He held Research Fellow positions at the Universities of Surrey and Cambridge before joining the University of Sheffield as a Lecturer in 1993, rising to his current position. He has published in excess of 200 peer reviewed papers and 3 books in the research areas of signal processing, system identification and control with applications in aerospace, manufacturing, life science and healthcare.

Professor Kadirkamanathan was awarded the PNAS Cozzarelli Prize in 2013. He has previously served as the Editor-in-Chief of the International Journal of Systems Science and as an Associated Editor of the IEEE Trans. Neural Networks.

Dr Charlotte Kemp graduated with a B.Sc (Hons) in Physics with Medical Physics in 2001 and a M.Sc. in Radiation Physics in 2004 from University College London, UK, followed by a Ph.D. in sleep and brain activity in 2008 from Loughborough University, UK. She is a Consultant Clinical Scientist and the Head of Clinical Engineering at Sheffield Teaching Hospitals NHS Foundation Trust. Charlotte has over 20 years' experience working in the NHS and is passionate about effective device innovation in healthcare and its application in improving patient care. She has five publications in peer-reviewed journals in the areas of medical device development and physiological measurements, numerous national and international presentations, including a TEDxNHS talk on innovation in the NHS in 2018, three intellectual property registrations (one patent, one registered design and one license) and was appointed as one of four Chief Scientific Office WISE (Women in Science and Engineering) Fellows nationally in 2016.